

# A NOVEL FIDELITY BASED ON THE ADAPTIVE DOMAIN FOR PANSHARPENING

Jin-Liang Xiao<sup>1</sup>Ting-Zhu Huang<sup>1,\*</sup>Liang-Jian Deng<sup>1,\*</sup>Ting Xu<sup>1</sup>

<sup>1</sup>School of Mathematical Sciences,  
University of Electronic Science and Technology of China, Chengdu, 611731, China

## ABSTRACT

Pansharpening aims to obtain the high resolution multispectral image (HRMS) using the panchromatic image (PAN) and low spatial resolution multispectral image (LRMS). The similarity between PAN and HRMS has shown powerful performance for spatial feature extraction. The prevailing methods usually describe the similarity on a fixed transformed domain. However, such domain, e.g., gradient domain, usually limits the preservation of spatial details and neglects flexibility. To overcome these challenges, we propose an adaptive transformed domain-based spatial fidelity to depict the similarity accurately and flexibly. Based on the proposed spatial fidelity, we build a novel variational pansharpening model that consists of spectral and spatial fidelity terms. We design an algorithm based on the alternating direction method of multiplier (ADMM) framework to solve the model. Experimental results on reduced- and full-resolution data verify the effectiveness of the proposed method.

**Index Terms**— Adaptive transformed domain, Spatial fidelity, Variational models, Pansharpening

## 1. INTRODUCTION

Remote sensing images have been widely applied in many fields such as soil investigation and vegetation monitoring [1]. Due to inevitable hardware limitations, satellites usually capture a pair of the panchromatic image (PAN) and low spatial resolution multispectral image (LRMS) simultaneously. *Pansharpening*, which stands for panchromatic sharpening, refers to fusing the above image pair to obtain the high resolution multispectral image (HRMS).

The pansharpening methods can be classified into four categories: component substitution (CS), multi-resolution analysis (MRA), deep learning (DL), and variational optimization (VO) methods. Classic CS and MRA approaches usually lead to spectral or spatial distortions. DL-based methods achieve satisfactory results on this problem. However, they require massive training data and often neglect interpretability [2]. VO-based methods have recently attracted much attention due to their powerful performance. These

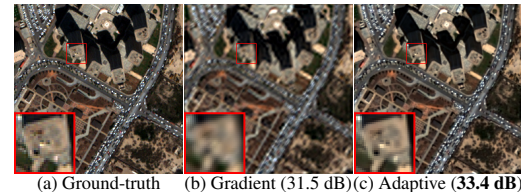


**Fig. 1.** The comparison among spatial features extracted from gradient and adaptive domains (value: PSNR).

methods address the pansharpening problem by constructing a variational model, typically incorporating spectral and spatial fidelity terms, such as those proposed in [3, 4].

More recently, the spatial fidelity based on the transformed domain has shown significant potential in leveraging the similarity between PAN and HRMS. The similarity has been characterized by projecting the residual of these two images onto the transformed domain. The existing methods usually choose the fixed transformed domain, e.g., gradient domain [5]. However, such transformed domain-based fidelity is fixed and not adaptable to the data, which limits the accuracy and flexibility for spatial features extraction.

To address these challenges, we propose a novel adaptive transformed domain-based spatial fidelity, which is adaptive to the inputs. In comparison to spatial fidelity based on the gradient domain, our proposed approach demonstrates enhanced accuracy, as illustrated in Fig. 1. The proposed domain can be iteratively updated according to the characteristics of the data. Leveraging the adaptive transformed domain-based spatial fidelity term, we formulate a novel variational pansharpening model and use alternating direction method of multiplier (ADMM) algorithm to solve it. The flexibility of the adopted transformed domain ensures that our method depicts the similarity between PAN and HRMS powerfully. Furthermore, the revision of the PAN is also helpful for the enhancement of the similarity (refer to (5) and (6)). The main contributions are summarized as follows:

- We propose a novel spatial fidelity term based on an adaptive transformed domain, which can depict the similarity between PAN and HRMS accurately.

- Based on the proposed adaptive-domain fidelity, we establish a new variational pansharpening model and use the ADMM algorithm to solve it. The proposed method is effective for spatial features extraction and provides flexibility with the data.
- Experiments on both reduced- and full-resolution datasets verify the effectiveness of the proposed method.

## 2. PROPOSED VARIATIONAL PANSHARPENING METHOD

### 2.1. Notations

In this paper, we denote tensors, matrices, vectors, and scalars as calligraphic bold capital letters, bold capital letters, bold lowercase letters, and lowercase letters, e.g.,  $\mathcal{X}$ ,  $\mathbf{X}$ ,  $\mathbf{x}$ , and  $x$ , respectively. We use  $\mathbf{I}$  to represent the identity matrix. For  $\mathbf{A} \in \mathbb{R}^{H \times W}$ ,  $\mathbf{A}(i_1, i_2)$  is the element in  $\mathbf{A}$  indexed by  $(i_1, i_2)$ , the Frobenius norm of  $\mathbf{A}$  is defined by  $\|\mathbf{A}\|_F = \sqrt{\sum_{i_1 i_2} \mathbf{A}(i_1, i_2)^2}$ . For  $\mathcal{A} \in \mathbb{R}^{H \times W \times S}$ ,  $\mathbf{A}^{(i)} \in \mathbb{R}^{H \times W}$  denotes the  $i$ -th frontal slice of  $\mathcal{A}$ , and  $\mathbf{A}_{(3)} \in \mathbb{R}^{S \times HW}$  represents mode-3 unfolding of  $\mathcal{A}$ .  $\mathcal{A} = \mathcal{M} \triangle \mathcal{N}$  means  $\mathbf{A}^{(i)} = \mathbf{M}^{(i)} \mathbf{N}^{(i)}$ ,  $i = 1, 2, \dots, S$ .  $(\cdot)^T$  and  $(\cdot)^{-1}$  represent the transpose and inverse operation, respectively.

### 2.2. Proposed Variational Pansharpening Model

The proposed variational pansharpening model includes two terms: the spectral fidelity term and the spatial fidelity term. We will introduce each term separately below.

#### 2.2.1. Spectral Fidelity

In general, LRMS  $\mathcal{Y} \in \mathbb{R}^{h \times w \times S}$  is considered as the spatial degraded version of HRMS  $\mathcal{X} \in \mathbb{R}^{H \times W \times S}$ , i.e.,  $\mathbf{Y}_{(3)} = \mathbf{X}_{(3)} \mathbf{B} \mathbf{S}$ . Therein,  $\mathbf{Y}_{(3)} \in \mathbb{R}^{S \times hw}$  and  $\mathbf{X}_{(3)} \in \mathbb{R}^{S \times HW}$  are the mode-3 unfolding of  $\mathcal{Y}$  and  $\mathcal{X}$ , respectively;  $\mathbf{B} \in \mathbb{R}^{HW \times HW}$  and  $\mathbf{S} \in \mathbb{R}^{HW \times hw}$  denote the spatial blurring matrix and down-sampling operator, respectively. Based on this, the spectral fidelity term is formulated as follows,

$$f_{spec} = \|\mathbf{X}_{(3)} \mathbf{B} \mathbf{S} - \mathbf{Y}_{(3)}\|_F^2, \quad (1)$$

where  $\|\cdot\|_F$  is Frobenius norm.

#### 2.2.2. Proposed Spatial Fidelity

The PAN mainly contains spatial features, thus VO-based methods usually extract spatial features from PAN. Since HRMS and PAN are spatially similar, therefore, the residual image of these two images should be sparse. Previous works tend to describe the residual of the HRMS and histogram-matched PAN [6]. However, there is a gap between the histogram-matched PAN and the target HRMS. In this paper,

**Table 1.** Results of different norms for sparsity on data from Tripoli dataset. (Bold: best; Underline: second best)

Norm for sparsity	PSNR $\uparrow$	SSIM $\uparrow$
$\ell_1$ -norm	33.41	0.920
$\ell_p$ -norm ( $0 < p < 1$ )	<u>33.60</u>	0.920
$\ell_0$ -norm	<b>33.76</b>	<u>0.923</u>

we revise PAN iteratively to enhance the sparsity of the residual. Based on the revised PAN, we propose a novel spatial fidelity term based on an *adaptive* transformed domain to characterize this sparsity, i.e.,

$$f_{spa} = \|\mathcal{W} \triangle \mathcal{X} - \mathcal{W} \triangle \mathcal{P}\|_0, \quad (2)$$

where  $\mathcal{P}$  is the revised PAN that is estimated by the least squares estimation (see (6)),  $\|\cdot\|_0$  is the  $\ell_0$ -norm,  $\mathcal{W} \in \mathbb{R}^{r \times H \times S}$  is an *adaptive* transformed tensor and satisfies  $\mathbf{W}^{(i)T} \mathbf{W}^{(i)} = \mathbf{I}, i = 1, \dots, S$ , and  $r$  is a fixed parameter of the transform.

The proposed spatial fidelity describes the similarity between PAN and HRMS. Compared with the gradient transformed domain, the adaptive domain is more flexible due to its iterative updating (please refer to (5) and (6)). Since the transform  $\mathcal{W}$  satisfies  $\mathbf{W}^{(i)T} \mathbf{W}^{(i)} = \mathbf{I}, i = 1, \dots, S$ , its inverse transform can be obtained conveniently, which avoid the complex computation like other domains.

Besides, the choice of the norm is vital for the constraint of sparsity. In previous works, the sparsity is usually constrained by  $\ell_1$ -norm and  $\ell_p$ -norm ( $0 < p < 1$ ) [7], which may influence the accuracy of the sparse constraint. In our model, we optimize  $\ell_0$ -norm to depict the sparsity. As shown in Table 1, the  $\ell_0$ -norm in our model achieves the best performance for the constraint of spatial details.

#### 2.2.3. Proposed Variational Pansharpening Model

We integrate the spectral fidelity (1) (which involves extracting spectral features from LRMS) and the spatial fidelity (2) (which involves extracting spatial features from PAN) to formulate a variational pansharpening model as follows:

$$\min_{\mathcal{X}} \|\mathbf{X}_{(3)} \mathbf{B} \mathbf{S} - \mathbf{Y}_{(3)}\|_F^2 + \lambda \|\mathcal{W} \triangle \mathcal{X} - \mathcal{W} \triangle \mathcal{P}\|_0, \quad (3)$$

where  $\lambda$  is a positive hyperparameter.

### 2.3. Solving Algorithm

We use the ADMM [14] to solve the proposed model (3). By introducing auxiliary variables  $\mathbf{U} = \mathbf{X}_{(3)} \mathbf{B}$  and  $\mathcal{V} = \mathcal{W} \triangle \mathcal{X} - \mathcal{W} \triangle \mathcal{P}$ , the augmented Lagrangian function concerning (3) is

$$\begin{aligned} L = & \|\mathbf{U} \mathbf{S} - \mathbf{Y}_{(3)}\|_F^2 + \frac{\eta_1}{2} \left\| \mathbf{X}_{(3)} \mathbf{B} - \mathbf{U} + \frac{\mathbf{G}_1}{\eta_1} \right\|_F^2 \\ & + \frac{\eta_2}{2} \left\| \mathcal{W} \triangle \mathcal{X} - \mathcal{W} \triangle \mathcal{P} - \mathcal{V} + \frac{\mathbf{G}_2}{\eta_2} \right\|_F^2 + \lambda \|\mathcal{V}\|_0, \end{aligned} \quad (4)$$

**Table 2.** Quantitative results for 42 images from Tripoli dataset. (Bold: best; Underline: second best)

Method	PSNR $\uparrow$	SSIM $\uparrow$	SAM $\downarrow$	SCC $\uparrow$	ERGAS $\downarrow$	Q8 $\uparrow$	Runtime (s) $\downarrow$
C-BDSD [8]	29.21 $\pm$ 3.069	0.875 $\pm$ 0.078	5.238 $\pm$ 1.835	0.900 $\pm$ 0.087	4.658 $\pm$ 2.607	0.879 $\pm$ 0.112	0.749 $\pm$ 0.035
RBDSD [9]	31.38 $\pm$ 1.664	0.889 $\pm$ 0.078	4.335 $\pm$ 1.741	0.939 $\pm$ 0.063	3.376 $\pm$ 1.497	0.897 $\pm$ 0.115	<b>0.054 <math>\pm</math> 0.004</b>
HMP [10]	30.95 $\pm$ 1.715	0.881 $\pm$ 0.071	4.372 $\pm$ 1.695	0.935 $\pm$ 0.064	5.351 $\pm$ 12.03	0.893 $\pm$ 0.106	0.139 $\pm$ 0.005
Reg-FS [6]	30.90 $\pm$ 1.633	0.876 $\pm$ 0.071	4.345 $\pm$ 1.722	0.936 $\pm$ 0.060	3.541 $\pm$ 1.452	0.886 $\pm$ 0.110	<u>0.105 <math>\pm</math> 0.005</u>
PNN [11]	27.87 $\pm$ 1.250	0.864 $\pm$ 0.067	6.141 $\pm$ 1.445	0.921 $\pm$ 0.060	5.231 $\pm$ 0.102	0.870 $\pm$ 0.102	0.281 $\pm$ 0.014
TPNN [12]	29.30 $\pm$ 1.529	0.848 $\pm$ 0.071	5.094 $\pm$ 1.683	0.925 $\pm$ 0.059	4.197 $\pm$ 1.320	0.865 $\pm$ 0.117	2.988 $\pm$ 0.193
CDIF [5]	31.90 $\pm$ 1.579	0.890 $\pm$ 0.073	4.049 $\pm$ 1.728	0.946 $\pm$ 0.057	3.168 $\pm$ 1.411	0.904 $\pm$ 0.106	30.96 $\pm$ 0.815
IMBD [13]	30.13 $\pm$ 1.816	0.862 $\pm$ 0.068	4.714 $\pm$ 1.713	0.930 $\pm$ 0.060	3.845 $\pm$ 1.451	0.877 $\pm$ 0.099	0.259 $\pm$ 0.023
Proposed	<b>32.13 <math>\pm</math> 1.679</b>	<b>0.896 <math>\pm</math> 0.068</b>	<u>3.972 <math>\pm</math> 1.773</u>	<b>0.948 <math>\pm</math> 0.056</b>	<u>3.094 <math>\pm</math> 1.426</u>	<b>0.910 <math>\pm</math> 0.100</b>	15.50 $\pm$ 0.061

where  $\eta_1$  and  $\eta_2$  are parameters,  $\mathbf{G}_1 \in \mathbb{R}^{S \times HW}$  and  $\mathcal{G}_2 \in \mathbb{R}^{r \times W \times S}$  are Lagrangian multipliers. Thus, the problem (4) is solved by alternately updating the following variables:

$$\left\{ \begin{array}{l} \mathcal{X}^{k+1} = \arg \min_{\mathcal{X}} \frac{\eta_1}{2} \left\| \mathbf{X}_{(3)} \mathbf{B} - \mathbf{U}^k + \frac{\mathbf{G}_1^k}{\eta_1} \right\|_F^2 \\ \quad + \frac{\eta_2}{2} \left\| \mathcal{W}^k \Delta \mathcal{X} - \mathcal{W}^k \Delta \mathcal{P}^k - \mathcal{V}^k + \frac{\mathcal{G}_2^k}{\eta_2} \right\|_F^2, \\ \mathcal{V}^{k+1} = \arg \min_{\mathcal{V}} \lambda \|\mathcal{V}\|_0 \\ \quad + \frac{\eta_2}{2} \left\| \mathcal{W}^k \Delta \mathcal{X}^{k+1} - \mathcal{W}^k \Delta \mathcal{P}^k - \mathcal{V} + \frac{\mathcal{G}_2^k}{\eta_2} \right\|_F^2, \\ \mathbf{U}^{k+1} = \arg \min_{\mathbf{U}} \left\| \mathbf{U} \mathbf{S} - \mathbf{Y}_{(3)} \right\|_F^2 \\ \quad + \frac{\eta_1}{2} \left\| \mathbf{X}_{(3)}^{k+1} \mathbf{B} - \mathbf{U} + \frac{\mathbf{G}_1^k}{\eta_1} \right\|_F^2, \\ \mathbf{G}_1^{k+1} = \mathbf{G}_1^k + \eta_1 (\mathbf{X}_{(3)}^{k+1} \mathbf{B} - \mathbf{U}^{k+1}), \\ \mathcal{G}_2^{k+1} = \mathcal{G}_2^k + \eta_2 (\mathcal{W}^k \Delta \mathcal{X}^{k+1} - \mathcal{W}^k \Delta \mathcal{P}^k - \mathcal{V}^{k+1}), \\ \mathbf{P}_{(3)}^{k+1} = \mathbf{H} \mathbf{P}_{(3)}^k, \\ \mathcal{W}^{k+1} = \arg \min_{\mathcal{W}} \left\| \mathcal{W} \Delta \mathcal{T}^{k+1} - \mathcal{V}^{k+1} + \frac{\mathcal{G}_2^{k+1}}{\eta_2} \right\|_F^2 \\ \quad + \frac{\rho}{2} \left\| \mathcal{W} - \mathcal{W}^k \right\|_F^2, \end{array} \right. \quad (5)$$

where  $\rho$  is a parameter,  $\mathcal{T}^{k+1} = \mathcal{X}^{k+1} - \mathcal{P}^{k+1}$ , and  $\mathbf{H} \in \mathbb{R}^{S \times S}$  is the revised operation that can be obtained by solving the following quadratic minimization problem:

$$\mathbf{H} = \arg \min_{\mathbf{H}} \left\| \mathbf{X}_{(3)}^{k+1} - \mathbf{H} \mathbf{P}_{(3)}^k \right\|_F^2. \quad (6)$$

Hence,  $\mathbf{H} = (\mathbf{X}_{(3)}^{k+1} (\mathbf{P}_{(3)}^k)^T) (\mathbf{P}_{(3)}^k (\mathbf{P}_{(3)}^k)^T)^{-1}$ . By this update of  $\mathbf{P}_{(3)}^k$ , the histogram-matched PAN is revised.

Especially, the optimization of  $\mathcal{X}^{k+1}$  and  $\mathcal{U}^{k+1}$  are two quadratic minimization problems. The solution of  $\mathcal{V}^{k+1}$  is obtained by a classic iterative method (please refer to [15]), which introduces two hyperparameters  $\alpha$  and  $\beta$ . Finally, we update the transformed tensor  $\mathcal{W}^k$  band-by-band, i.e.,

$$(\mathbf{W}^k)^{(i)} = \mathbf{E}^{(i)} \mathbf{F}^{(i)T}, \quad i = 1, \dots, S, \quad (7)$$

where  $\mathbf{E}^{(i)} \Sigma^{(i)} (\mathbf{F}^{(i)})^T$  is the singular value decomposition of  $(\mathbf{V}^{k+1} - \frac{\mathbf{G}_2^{k+1}}{\eta_2})^{(i)} ((\mathbf{X}^{k+1} - \mathbf{P}^{k+1})^{(i)T} + \rho (\mathbf{W}^k)^{(i)T})$  (refer to [16]). Overall, the algorithm has seven parameters, i.e.,  $\lambda$ ,  $\eta_1$ ,  $\eta_2$ ,  $\rho$ ,  $\alpha$ ,  $\beta$ ,  $r$ , that need to be adjusted for better performance.

### 3. NUMERICAL EXPERIMENTS

In this section, we conduct a comparative analysis of the proposed method against state-of-the-art methods on reduced- and full-resolution data. Moreover, we make the ablation study to verify the effectiveness of the proposed fidelity.

**Benchmark and Platform.** Compared methods include C-BDSD [8], RBDSD [9], HPM [10], Reg-FS [6], PNN [11], TPNN [12], CDIF [5], and IMBD [13]. All the methods are conducted on PC with MATLAB (R2020a), Intel(R) Core(TM) i9-12900K 3.20 GHz, RAM 64 GB, and NVIDIA GeForce GTX 1650. It is noteworthy that all DL methods utilize the pretrained models.

**Datasets and Quantitative Metrics.** We choose the Tripoli dataset (size of the PAN: 256  $\times$  256, source: WorldView-3 satellite) and Stockholm dataset (size of the PAN: 400  $\times$  400, source: WorldView-2 satellite) for reduced- and full-resolution comparisons, respectively. We apply the peak signal-to-noise ratio (PSNR), the structural similarity index (SSIM) [17], the spectral angle mapper (SAM) [18], the spatial correlation coefficient (SCC) [19], the erreur relative globale adimensionnelle de synthèse (ERGAS) [20], Q8 [21] metric for reduced-resolution data. Besides, the quality with no reference (QNR) [22], which consists of a spectral quality index  $D_\lambda$  and a spatial quality index  $D_s$ , is employed for full-resolution data. We also compared the computational efficiency of the methods by measuring the runtime in seconds.

#### 3.1. Experimental Results on Reduced-Resolution Data

**Quantitative Comparison.** The results on the 42 images from Tripoli dataset are presented in Table 2. As depicted in this table, the proposed method achieves better quality results than other methods. The runtime of the proposed method is less than that of the CDIF. Note that the compared method, i.e., CDIF, is a VO-based method. The spatial fidelity in the method is different from the one in our proposed method. The quantitative results indicate the superiority of the proposed spatial fidelity based on the adaptive domain.

**Visual Comparison.** To offer a comprehensive evaluation of the pansharpening results among the methods, we extend the quality assessment to visual perception. Color images of the reconstructed Tripoli dataset along with their error images are shown in Fig. 2. The representative regions in these images

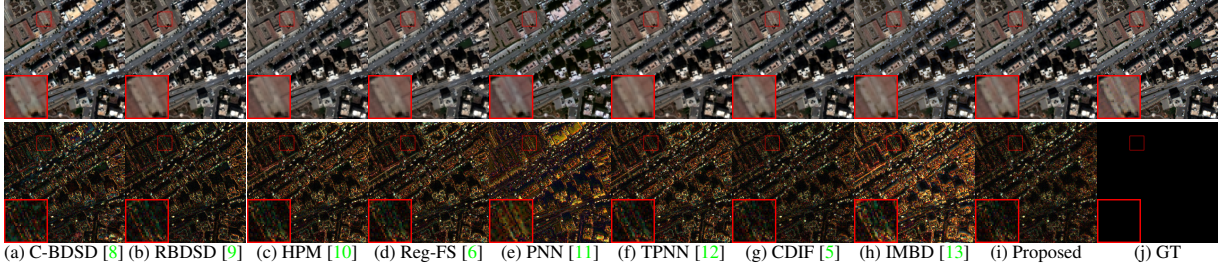


**Fig. 2.** Top: Color images consisting of the 5th (R), 3rd (G), and 2nd (B) bands of the fused Tripoli dataset (reduced resolution), generated by (a) C-BDSD, (b) RBDSD, (c) HPM, (d) Reg-FS, (e) PNN, (f) TPNN, (g) CDIF, (h) IMBD, (i) proposed, and (j) GT. Bottom: The corresponding error images, enhanced by multiplying by a fixed number (i.e., 8).

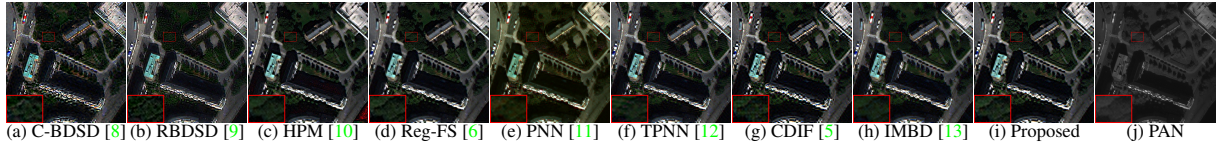


**Fig. 3.** Color images consisting of the 5th (R), 3rd (G), and 2nd (B) bands of the Stockholm dataset (full resolution), generated by (a) C-BDSD, (b) RBDSD, (c) HPM, (d) Reg-FS, (e) PNN, (f) TPNN, (g) CDIF, (h) IMBD, (i) Proposed, and (j) PAN.

**Table 3.** Quantitative results for 8 images from Stockholm dataset.  
(Bold: best; Underline: second best)

Method	$D_{\lambda} \downarrow$	$D_s \downarrow$	QNR $\uparrow$	Runtime (s) $\downarrow$
C-BDSD [8]	0.119 $\pm$ 0.035	0.203 $\pm$ 0.037	0.702 $\pm$ 0.050	0.938 $\pm$ 0.129
RBDSD [9]	0.026 $\pm$ 0.009	0.042 $\pm$ 0.011	0.933 $\pm$ 0.015	<b>0.113 <math>\pm</math> 0.071</b>
HPM [10]	0.050 $\pm$ 0.015	0.047 $\pm$ 0.016	0.905 $\pm$ 0.028	0.162 $\pm$ 0.014
Reg-FS [6]	0.059 $\pm$ 0.015	0.058 $\pm$ 0.016	0.887 $\pm$ 0.028	0.114 $\pm$ 0.008
PNN [11]	0.054 $\pm$ 0.005	0.037 $\pm$ 0.008	0.911 $\pm$ 0.009	0.453 $\pm$ 0.682
TPNN [12]	0.033 $\pm$ 0.009	<b>0.029 <math>\pm</math> 0.010</b>	0.939 $\pm$ 0.012	2.469 $\pm$ 0.483
CDIF [5]	0.034 $\pm$ 0.004	0.060 $\pm$ 0.010	0.908 $\pm$ 0.012	55.31 $\pm$ 0.740
IMBD [13]	<b>0.019 <math>\pm</math> 0.002</b>	0.061 $\pm$ 0.013	0.922 $\pm$ 0.014	1.356 $\pm$ 0.014
Proposed	0.030 $\pm$ 0.007	0.031 $\pm$ 0.007	<b>0.940 <math>\pm</math> 0.007</b>	24.18 $\pm$ 0.062

are highlighted by red boxes. Among all the methods, the proposed one achieves the least error, which demonstrates the advantages of the proposed method on the problem.

### 3.2. Experimental Results on Full-Resolution Data

**Quantitative Comparison.** To further demonstrate the effectiveness of the proposed method, we execute all methods on the Stockholm full-resolution dataset. The quantitative results on the 8 images from the Stockholm full-resolution dataset are presented in Table 3. The proposed method has the best value for QNR, and its runtime is less than the CDIF.

**Visual Comparison.** For visual performance, we present an image of the reconstructed Stockholm data shown in Fig. 3. The representative regions in these images are highlighted by red boxes. From this figure, we observe that the proposed method is closest to the PAN, demonstrating its effectiveness on full-resolution pansharpening results.

### 3.3. Ablation Study

The proposed final model (3) consists of the spectral fidelity (1) and the proposed spatial fidelity (2). We conduct

**Table 4.** Ablation experiment results on data from Tripoli dataset.  
(Bold: best; Underline: second best)

Spectral Fidelity	Spatial Fidelity	PSNR $\uparrow$	SSIM $\uparrow$
✓		27.67	0.650
	✓	30.23	0.890
✓	✓	<b>33.74</b>	<b>0.923</b>

further experiments on an image from the Tripoli dataset to test the performance of these two fidelity terms. We use PSNR and SSIM to measure accuracy. The results are presented in Table 4. From this table, the proposed model with both spectral and spatial fidelities achieves the best results.

## 4. CONCLUSION

In this paper, we proposed an adaptive domain-based spatial fidelity for variational pansharpening. We proposed a novel spatial fidelity based on the adaptive transformed domain, which can better depict the similarity between PAN and HRMS compared to the gradient domain. Based on the proposed spatial fidelity, we designed a variational pansharpening model. We used the ADMM-based algorithm to solve the model. Experiments on reduced- and full-resolution datasets demonstrated the effectiveness of the proposed method compared with current state-of-the-art pansharpening methods.

## 5. ACKNOWLEDGEMENTS

This work is supported by NSFC (12171072 and 12271083), Natural Science Foundation of Sichuan Province (2022NSFSC0501), Key Projects of Applied Basic Research in Sichuan Province (2020YJ0216), and National Key Research and Development Program of China (2020YFA0714001).

## 6. REFERENCES

- [1] H. Zhang, He. Wang, X. Tian, and J. Ma, “P2sharpener: A progressive pansharpening network with deep spectral transformation,” *Inf. Fusion*, vol. 91, pp. 103–122, 2023.
- [2] L.-J. Deng, G. Vivone, M. E. Paoletti, G. Scarpa, J. He, Y. Zhang, J. Chanussot, and A. Plaza, “Machine learning in pansharpening: A benchmark, from shallow to deep networks,” *IEEE Geosci. Remote Sens. Mag.*, vol. 10, no. 3, pp. 279–315, 2022.
- [3] R. Wen, L.-J. Deng, Z.-C. Wu, X. Wu, and G. Vivone, “A novel spatial fidelity with learnable nonlinear mapping for panchromatic sharpening,” *IEEE Trans. Geosci. Remote Sens.*, vol. 61, pp. 1–15, 2023.
- [4] Z.-C. Wu, T.-Z. Huang, L.-J. Deng, J. Huang, J. Chanussot, and G. Vivone, “LRTCFPan: Low-rank tensor completion based framework for pansharpening,” *IEEE Trans. Image Process.*, vol. 32, pp. 1640–1655, 2023.
- [5] J.-L. Xiao, T.-Z. Huang, L.-J. Deng, Z.-C. Wu, and G. Vivone, “A new context-aware details injection fidelity with adaptive coefficients estimation for variational pansharpening,” *IEEE Trans. Geosci. Remote Sens.*, vol. 60, pp. 1–15, 2022.
- [6] G. Vivone, R. Restaino, and J. Chanussot, “Full scale regression-based injection coefficients for panchromatic sharpening,” *IEEE Trans. Image Process.*, vol. 27, no. 7, pp. 3418–3431, 2018.
- [7] L.-J. Deng, M. Feng, and X.-C. Tai, “The fusion of panchromatic and multispectral remote sensing images via tensor-based sparse modeling and hyper-Laplacian prior,” *Inf. Fusion*, vol. 52, pp. 76–89, 2019.
- [8] A. Garzelli, “Pansharpening of multispectral images based on nonlocal parameter optimization,” *IEEE Trans. Geosci. Remote Sens.*, vol. 53, no. 4, pp. 2096–2107, 2014.
- [9] G. Vivone, “Robust band-dependent spatial-detail approaches for panchromatic sharpening,” *IEEE Trans. Geosci. Remote Sens.*, vol. 57, no. 9, pp. 6421–6433, 2019.
- [10] G. Vivone, R. Restaino, M. Dalla Mura, G. Licciardi, and J. Chanussot, “Contrast and error-based fusion schemes for multispectral image pansharpening,” *IEEE Geosci. Remote Sens. Lett.*, vol. 11, no. 5, pp. 930–934, 2013.
- [11] G. Masi, D. Cozzolino, L. Verdoliva, and G. Scarpa, “Pansharpening by convolutional neural networks,” *Remote Sens.*, vol. 8, no. 7, pp. 594, 2016.
- [12] G. Scarpa, S. Vitale, and D. Cozzolino, “Target-adaptive CNN-based pansharpening,” *IEEE Trans. Geosci. Remote Sens.*, vol. 56, no. 9, pp. 5443–5457, 2018.
- [13] H. Lu, Y. Yang, S. Huang, X. Chen, H. Su, and W. Tu, “Intensity mixture and band-adaptive detail fusion for pansharpening,” *Pattern Recognit.*, vol. 139, pp. 109434, 2023.
- [14] S. Boyd, N. Parikh, E. Chu, B. Peleato, and J. Eckstein, “Distributed optimization and statistical learning via the alternating direction method of multipliers,” *Mach. Learn.*, vol. 3, no. 1, pp. 1–122, 2011.
- [15] G. Yuan and B. Ghanem, “ $\ell_0$ TV: a sparse optimization method for impulse noise image restoration,” *IEEE Trans. Pattern Anal. Mach. Intell.*, vol. 41, no. 2, pp. 352–364, 2019.
- [16] T. Xu, T.-Z. Huang, L.-J. Deng, and N. Yokoya, “An iterative regularization method based on tensor subspace representation for hyperspectral image super-resolution,” *IEEE Trans. Geosci. Remote Sens.*, vol. 60, pp. 1–16, 2022.
- [17] Z. Wang, A. C. Bovik, H. R. Sheikh, and E. P. Simoncelli, “Image quality assessment: from error visibility to structural similarity,” *IEEE Trans. Image Process.*, vol. 13, no. 4, pp. 600–612, 2004.
- [18] R. H. Yuhas, A. F. H. Goetz, and J. W. Boardman, “Discrimination among semi-arid landscape endmembers using the spectral angle mapper (SAM) algorithm,” in *Proc. Summaries 3rd Annu. JPL Airborne Geosci. Workshop*, 1992, vol. 1, pp. 147–149.
- [19] X. Otazu, M. González-Audícan, O. Fors, and J. Núñez, “Introduction of sensor spectral response into image fusion methods. application to wavelet-based methods,” *IEEE Trans. Geosci. Remote Sens.*, vol. 43, no. 10, pp. 2376–2385, 2005.
- [20] L. Alparone, L. Wald, J. Chanussot, C. Thomas, P. Gamba, and L. M. Bruce, “Comparison of pansharpening algorithms: Outcome of the 2006 GRS-S data-fusion contest,” *IEEE Trans. Geosci. Remote Sens.*, vol. 45, no. 10, pp. 3012–3021, 2007.
- [21] A. Garzelli and F. Nencini, “Hypercomplex quality assessment of multi/hyperspectral images,” *IEEE Geosci. Remote Sens. Lett.*, vol. 6, no. 4, pp. 662–665, 2009.
- [22] L. Alparone, B. Aiazzi, S. Baronti, A. Garzelli, F. Nencini, and M. Selva, “Multispectral and panchromatic data fusion assessment without reference,” *Photogramm. Eng. Remote Sens.*, vol. 74, no. 2, pp. 193–200, 2008.